2021 IEEE 17th International Conference on Automation Science and Engineering (CASE)
August 23-27, 2021. Lyon, France

Automated Robotic Assembly of 3D Mesostructure via Guided Mechanical Buckling

Ying Cai, Zhonghao Han, Trey Cranney, Hangbo Zhao, and Satyandra K. Gupta*

***Abstract*— We present an automated assembly approach to forming 3D mesostructures using guided mechanical buckling of patterned thin films. This task requires accurate positioning of mesostructures over large distances. We use an industrial robot with a high degree of repeatability and large reach. We utilize image-guided localization and positioning to enable accurate pick and place of mesoscale thin films, dispensing of nanoliter adhesive in targeted regions, and automatic 2D to 3D shape transformation via mechanical buckling. We achieved the positioning accuracy of 80 μm, as demonstrated in the example of automated mechanical assembly of 3D mesostructures. The positioning accuracy could be further improved by enhancing the positioning accuracy of the robot, increasing the image resolution and optimizing the assembly process. The use of industrial robots with image-guided localization and positioning provides potential opportunities for high-accuracy, low-cost, and complex robotic manipulation at meso- and microscale.**

I. Introduction

The development of three-dimensional (3D) manufacturing of advance materials with feature sizes in the mesoscopic range (between tens of nanometers and hundreds of micrometers) has attracted growing interests, driven by the potential utility of 3D mesostructures in a wide range of functional systems such as microelectromechanical systems (MEMS), biomedical devices, energy storage and conversion platforms, and optical/optoelectronic components [1]. The most successful approaches of manufacturing 3D mesostructures include top-down techniques based on micromachining and microfabrication-based material removal, and bottom-up techniques such as 3D printing. As alternatives to these top-down and bottom-up approaches, 3D mesostructures can be realized by mechanically-directed, two-dimensional (2D) to 3D shape transformations processes where mechanical buckling induced by deformation of an elastomeic substrate geometrically transforms planar structures into complex 3D architectures [2], [3]. Such scheme enables the production of 3D geometries in nearly any type of materials, across lengthscales from nanoscale to macroscale, and with a rich diversity of complex shapes (see examples in Fig. 1). Potential applications of these 3D mesostructures include energy harvesting [4], metamaterials [5], and tissue engineering [6]–[8].

The guided mechanical assembly process typically starts with patterning thin film materials in planar formats (referred to as "2D precursors") using microfabrication or micromachining techniques, followed by defining specific regions on these 2D precursors to bond with a prestretched elastomeric substrate through patterned surface functionalization both on the 2D precursors and the substrate. Release of the prestretched substrate exerts compressive forces to the 2D precursors, thereby transforming them into 3D structures through spatially dependent in- and out-of-plane translational and rotational motions. While this scheme features parallel operation that enables the formation of 3D mesostructures from large arrays of 2D precursors in a one-step buckling process, limitations remain in the throughput of this approach, imposed mainly by steps that lie outside of standard microfabrication. These steps include patterned surface functionalization of bonding sites and elastomeric substrate typically via surface plasma treatment through shadow masking, and bonding of 2D precursors on the substrate with spatial alignment. Currently these steps require certain levels of manual operation, especially the alignment of shadow masking on 2D precursors, picking up, placement and bonding of 2D precursors onto the substrate. Automation of these steps allows for fully scalable formation of 3D mesostructures from 2D precursors, thereby avoiding the requirement of manual intervention and significantly increasing the throughput, quality, and consistency during large-scale manufacturing of functional 3D mesostructures.

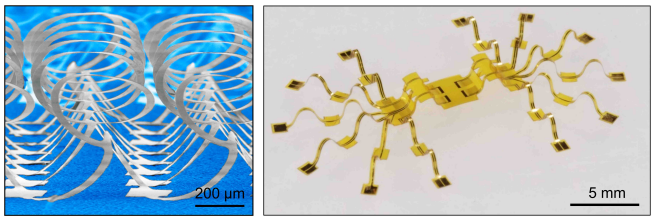

Fig. 1: Examples of 3D mesostructures formed by guided mechanical assembly: 3D silicon helix structures (left) [2] and 3D electronic sensors (right) [8].

Automation technology for this process needs to meet the following three requirements. First, we need to achieve high placement accuracy to ensure that assembly operations at small size scale are successful. Second, the process requires moving small components over large (meter scale) distances. Third, we want to achieve automation with commercially available low-cost technology.

One potential route to automating the above-mentioned steps is to utilize industrial robotic manipulators. These manipulators have a long reach, and provide high repeatability. Mass produced industrial manipulators are cost effective and highly reliable [9]. However, most robotic manipulators do not have high accuracy. we believe that image-guided localization and positioning can be be used to achieve the desired level of accuracy automate the 3D assembly process. Specif-

*Address all correspondence to this author.
Department of Aerospace and Mechanical Engineering, University of Southern California, CA USA 90089; Center for Advanced Manufacturing, University of Southern California, CA USA 90007 [guptask]@usc.edu

2021 IEEE 17th International Conference on Automation Science and Engineering (CASE) | 978-1-6654-1873-7/21/$31.00 ©2021 IEEE | DOI: 10.1109/CASE49439.2021.9551609

ically, bonding between 2D precursors and the substrate in spatially selective regions is achievable by precise dispensing of adhesives on the bonding sites of 2D precursors; handling of the 2D precursors and the bonding operation could be executed by robots. Image-guided localization and positioning plays an essential role in robotic manufacturing at small scales due to their applications in precise positioning and manipulation [10]–[12]. It can enable accurate detection and positioning of 2D precursors with bonding sites well within sub-millimeter errors, thereby enabling industrial robots to perform the assembly procedures at meso- or microscale.

II. Related Work

Automated assembly at micro- and mesoscale has been demonstrated in various systems that rely primarily on vision-based multi-axis motion stages [13]. Examples include automated micro-transfer printing which involves pick and place of micro- and mesoscale electronic devices [14], assembly of microscale objects using probes [15], [16], assembly of flexible optical components using microgrippers [17], and mesoscale soldering operations [18]. While some of these systems allow assembly at small scales with sufficient accuracy, limitations exist in the degrees of freedom allowable for complex manipulation in 3D space, the range of motion, as well as the difficulty and costs associated with building customized precision motion systems.

The use of industrial robots integrated with machine vision for small-scale assembly has been relatively less reported. Ruggeri *et al.* reported a vision-based robotized micro-manipulation and assembly work-cell for printed circuit board manufacturing [19]. The tasks involve precise positioning of surface-mounted electronics components, soldering, inspection and control of the task success. Niu *et al.* reported an automatic assembly system, consisting of a 6 degrees of freedom (DOF) industrial robot and a three-camera vision system [20]. One eye-in-hand camera is used for object detection and pose estimation during pick and place operations, and two other fixed cameras are for assembly verification. This multi-camera machine vision system is used to demonstrate the assembly of a pocket calculator using millimeter and centimeter components. A similar system that incorporates a force sensor at the end effector has been reported for assembly of millimeter-sized objects via aligning, grasping, and inserting operations [21]. In the multi-camera configuration, one camera with large field of view is installed on the robotic end effector to guide robot to locate components in large working space. Two microscopic cameras with small field of view and high resolution are used to measure the pose errors of components in aligning stage for assembly.

III. Experimental Setup and Procedure

We decompose the automated assembly process into four steps: 1) picking up 2D precursors, 2) dispensing of adhesives, 3) bonding of 2D precursors and prestretched substrates, and 4) mechanical buckling of 2D precursors to form 3D structures. Schematic illustration of the process appears in Fig. 2.

Fig. 3 shows the overall experimental setup consisting of the following main components: a 6 DOF industrial robot (Motoman GP8, Yaskawa), an adhesive dispenser (Ultimus II, Nordson EFD), a camera (U3-3800CP-M/C, IDS Imaging) with a lens (CF50ZA-1S, FUJIFILM) and a custom automatic stretcher. Detailed experimental procedures are described below. A video of the assembly process appears in [22].

1) Picking of 2D precursors

The picking of pre-patterned polyimide (PI) 2D precursors formed by laser cutting (thickness: 12.7 μm) is facilitated by a polydimethylsiloxane (PDMS) stamp (approximately 2 cm x 2 cm) mounted on the robot end effector inside a trapezoidal frame. 2D precursors are picked up by the PDMS stamp from a glass substrate covered by an adhesive film (Gel-Pak) with gentle pressure, due to the stronger adhesion between the PI and PDMS as compared to that between the PI and the adhesive film. Due to the variations of 2D precursor locations on the glass substrate, there is large variability on the locations of 2D precursors on the stamp after picking up, which can be in the order of few mm.

2) Dispensing of adhesive on bonding sites

A UV-curable adhesive (Henkel Loctite 5055 or RapidFix UV liquid plastic adhesive) is chosen for bonding the 2D precursors to a silicone (Dragon Skin, Smooth-On) or urethane (VytaFlex 30, Smooth-On) rubber substrate. A high-precision benchtop fluid dispenser connected to a syringe barrel with a tip (diameter: 100 μm) is used for dispensing the adhesive. A fixed camera next to the fluid dispenser provides vision to support localizing 2D precursors on the stamp. Details of the image-guided localization and positioning are discussed in Section IV.

3) Bonding of 2D precursors to elastomeric substrates

Upon dispensing of the UV-curable adhesive on the bonding sites of 2D precursors, the PDMS stamp is brought to the the automatic stretcher by the robot with a travel distance of approximately 1 m and placed onto the prestretched silicone substrate under gentle contact. A brief exposure of the adhesive to a UV LED underneath the prestretched substrate cures the adhesive, forming a strong bonding between the 2D precursors and the substrate. Lifting the stamp completes the bonding process.

4) Stretching and release of elastomeric substrates

A custom stretcher allows for automatic biaxial stretching and release of the assembly substrate with precise displacements. The key components are four pneumatic grippers amounted onto linear traversal actuators, which have a travel distance of 100 mm and repeatability of 0.3 mm. The pneumatic control of the opening and closing of grippers and the electric control of the motion of linear traversals are realized by a microcontroller (Arduino Mega 2560).

IV. Image Guided Localization and Positioning

A. Localization of 2D precursors on the stamp

A representative 2D precursor pattern is a cross with four circular bonding sites as shown in Fig. 4. To obtain the 2D

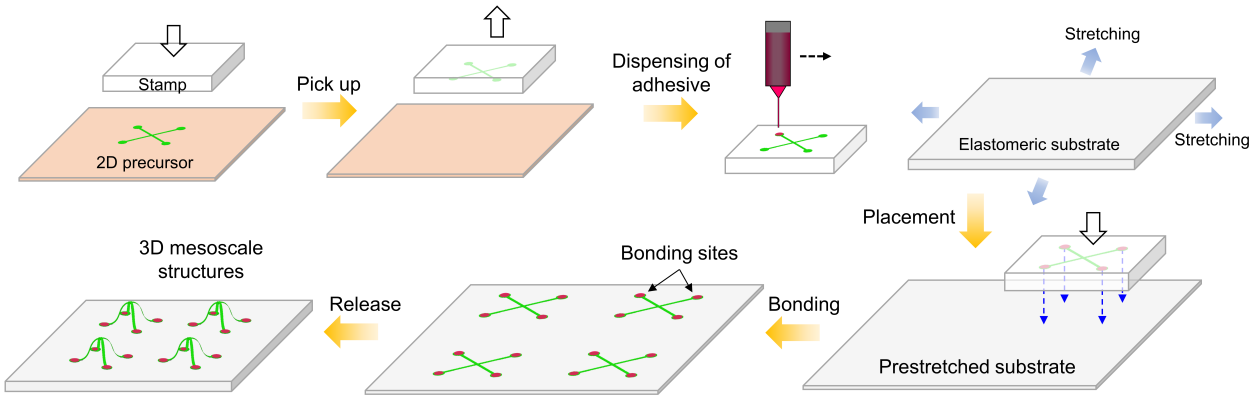

Fig. 2: Schematic illustration of the assembly process for forming 3D mesostructures.

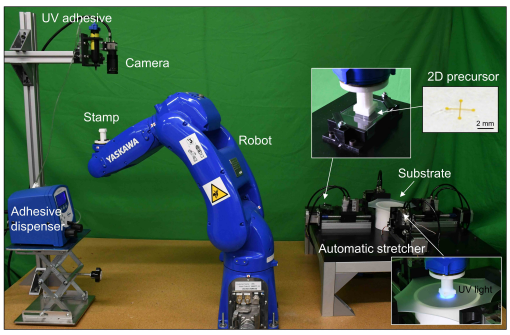

Fig. 3: Experimental setup for automated assembly of 3D mesostructures by mechanical buckling.

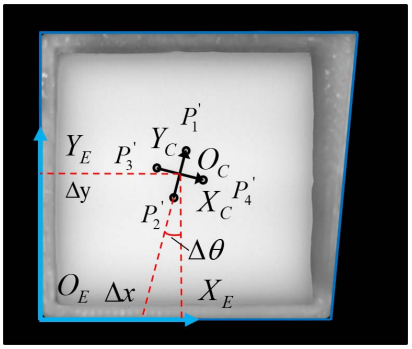

Fig. 4: Localization of the 2D precursor from images captured by the camera.

precursor's pose relative to the robot, the camera vision (9.6 μm/pixel) is used to detect the trapezoidal end effector's four edges and the 2D precursor's four circular bonding sites denoted as $\boldsymbol{P_1'}$, $\boldsymbol{P_2'}$, $\boldsymbol{P_3'}$, $\boldsymbol{P_4'}$, respectively. The end effector and 2D precursor are in the same plane during the localization process.

The image processing includes the following steps. We apply thresholding to separate out the region of the end effector and the Canny edge detection operation to extract its edges, followed by the use of the Hough transform to detect the four lines of the trapezoidal edges. For the 2D precursor, after the noise is removed by the Median Blur operation, the Hough transform is used to detect the circular edges of the bonding sites.

Based on the localization results, frame $\{\boldsymbol{E}\}$ for the end effector and frame $\{\boldsymbol{C}\}$ for the 2D precursor can be established (Fig. 4).

The relationship between frame $\{\boldsymbol{E}\}$ and frame $\{\boldsymbol{C}\}$ is

$$\boldsymbol{T_C^E} = transl(\Delta x, \Delta y, 0) rotz(\Delta\theta) \tag{1}$$

where Δx, Δy and $\Delta\theta$ can be calculated according to the camera's perspective projection model (Fig. 5). Fig. 5 describes the relationships between the world frame $\{\boldsymbol{W}\}$, the camera frame $\{\boldsymbol{L}\}$, the image plane frame $\{\boldsymbol{I}\}$, and the pixel frame $\{\boldsymbol{P}\}$. Based on the relationships, Δx, Δy and

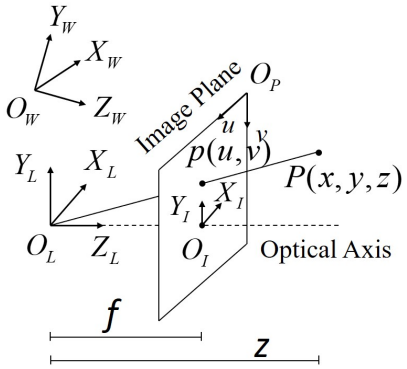

Fig. 5: Camera's perspective projection model.

$\Delta\theta$ can be estimated as

$$\begin{aligned} \Delta x = \tfrac{dx}{f} z \Delta u, \Delta y = \tfrac{dy}{f} z \Delta v \\ \cos\Delta\theta = \frac{\boldsymbol{P_2'P_1'} \cdot \boldsymbol{O_E Y_E}}{\|\boldsymbol{P_2'P_1'}\| \|\boldsymbol{O_E Y_E}\|} \end{aligned} \tag{2}$$

where $\frac{dx}{f}$ and $\frac{dy}{f}$ are parameters from the camera's intrinsic matrix, Δu and Δv are the deviations between $\boldsymbol{O_E}$ and $\boldsymbol{O_C}$ along the $\boldsymbol{u}$ and $\boldsymbol{v}$ axes in pixel frame $\{\boldsymbol{P}\}$, respectively. z can be estimated by

$$z = \frac{S_r}{S_I} f \tag{3}$$

where S_r denotes the area of the quadrilateral surrounded by$\boldsymbol{P_1'}$, $\boldsymbol{P_2'}$, $\boldsymbol{P_3'}$ and $\boldsymbol{P_4'}$ in the world frame $\{\boldsymbol{W}\}$ or the camera's frame $\{\boldsymbol{L}\}$, S_I denotes the area of a quadrilateral

surrounded by $\boldsymbol{P_1'}$, $\boldsymbol{P_2'}$, $\boldsymbol{P_3'}$ and $\boldsymbol{P_4'}$ in the camera's image plane frame $\{\boldsymbol{I}\}$. f is the lens' focal length (50 mm). Thus, through the detection of the 2D precursor and the end effector, the transformation matrix $\boldsymbol{T_C^E}$ from the end effector to the 2D precursor can be obtained. This step localizes the 2D precursor within the end effector.

B. Positioning of 2D precursors

In order to position 2D precursors under the dispenser, we need to localize the dispenser with respect to the end effector. We solve this problem indirectly by introducing a calibration step to acquire a reference location. The robot with the PDMS stamp is first driven manually under the dispensing tip, followed up dispensing of a drop of adhesive with a volume of approximately 2 nL on the PDMS stamp. The joint values of the robot $\boldsymbol{\theta_R}$ and the location of the adhesive drop on the PDMS stamp $\boldsymbol{P_R}$ are recorded (Fig. 6). $\boldsymbol{\theta_R}$ and $\boldsymbol{P_R}$ are set as the references.

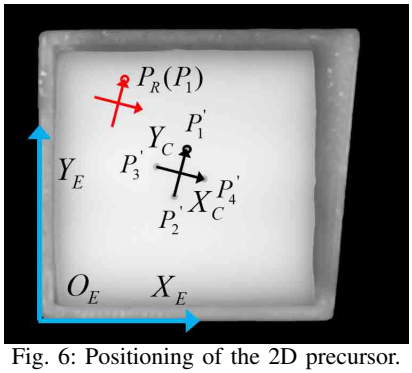

Fig. 6: Positioning of the 2D precursor.

For correctly driving the robot to the position for dispensing adhesive on the bonding sites, a mapping relationship from $\boldsymbol{T_C^R}$ to $\boldsymbol{\Delta\theta}$ is established. Here $\boldsymbol{T_C^R}$ is the transformation matrix from the adhesive reference $\boldsymbol{P_R}$ to the 2D precursor $\{\boldsymbol{C}\}$ and $\boldsymbol{\Delta\theta}$ stands for the differential values between the target joint values $\boldsymbol{\theta_T}$ and reference joint values $\boldsymbol{\theta_R}$.

Using the bonding site $\boldsymbol{P_1'}$ in Fig. 6 as an example, we set an imaginary 2D precursor, whose $\boldsymbol{P_1}$ is set as reference $\boldsymbol{P_R}$, with the same direction as in frame $\{\boldsymbol{C}\}$. The imaginary 2D precursor $\{\boldsymbol{R_1}\}$ is referred to as the reference 2D precursor for bonding site $\boldsymbol{P_1'}$. Then equations 1, 2 and 3 can be applied to calculate $\boldsymbol{T_{R_1}^E}$ and $\boldsymbol{T_C^{R_1}}$. The transformation matrix that carries the 2D precursor $\{\boldsymbol{C}\}$ to the target dispensing location $\boldsymbol{T_E^0(\theta_{T_1})}$ can be calculated as

$$\boldsymbol{T_E^0(\theta_{T_1})} = \boldsymbol{T_E^0(\theta_R)T_{R_1}^E(T_{R_1}^E T_C^{R_1})^{-1}} \tag{4}$$

According to robotic forward kinematics, given $\boldsymbol{\theta_R}$, we have

$$\boldsymbol{T_E^0(\theta_R)} = \boldsymbol{T_6^0(\theta_R)T_E^6} \tag{5}$$

where $\boldsymbol{T_E^6}$ is the transformation matrix from the robotic $\{\boldsymbol{6}\}$ frame to the end effector frame $\{\boldsymbol{E}\}$, which is a constant. $\boldsymbol{T_i^0}, i = 0, 2, ..., 6$ stands for the transformation matrix from the robotic $\{\boldsymbol{0}\}$ frame to the $\{\boldsymbol{i}\}$ frame (see Fig. 7) which can be written as

$$\boldsymbol{T_i^0} = \begin{bmatrix} \boldsymbol{x_i^0} & \boldsymbol{y_i^0} & \boldsymbol{z_i^0} & \boldsymbol{o_i^0} \\ 0 & 0 & 0 & 1 \end{bmatrix} \tag{6}$$

$\boldsymbol{T_6^0(\theta_R)}$ and $\boldsymbol{T_6^0(\theta_{T_1})}$ can be also expressed as

$$\begin{aligned} \boldsymbol{T_6^0(\theta_R)} =& transl(x_R, y_R, z_R) \\ & \times rotz(\theta_{ZR2})roty(\theta_{YR})rotz(\theta_{ZR1}) \end{aligned} \tag{7}$$

$$\begin{aligned} \boldsymbol{T_6^0(\theta_{T_1})} =& transl(x_{T_1}, y_{T_1}, z_{T_1}) \\ & \times rotz(\theta_{ZT_12})roty(\theta_{YT_1})rotz(\theta_{ZT_11}) \end{aligned} \tag{8}$$

where θ_{ZR1}, θ_{YR} and θ_{ZR2} (or θ_{ZT_11}, θ_{YT_1} and θ_{ZT_12}) are $\boldsymbol{ZYZ}$ Euler angles of frame$\{\boldsymbol{6}\}$, with respect to the robot's frame $\{\boldsymbol{0}\}$; x_R, y_R and z_R (or x_{T_1}, y_{T_1} and z_{T_1}) are the translations of robotic frame$\{\boldsymbol{6}\}$ relative to frame$\{\boldsymbol{0}\}$ along the $\boldsymbol{X}$, $\boldsymbol{Y}$, and $\boldsymbol{Z}$ axes. From the equations 7 and 8 above, we can obtain

$$\boldsymbol{V_R} = [x_R, y_R, z_R, \theta_{ZR1}, \theta_{YR}, \theta_{ZR2}]^T \tag{9}$$

$$\boldsymbol{V_{T_1}} = [x_{T_1}, y_{T_1}, z_{T_1}, \theta_{ZT_11}, \theta_{YT_1}, \theta_{ZT_12}]^T \tag{10}$$

Therefore, we have

$$\boldsymbol{\Delta V_1} = \boldsymbol{V_{T_1}} - \boldsymbol{V_R} \tag{11}$$

For calculating $\boldsymbol{\Delta\theta_1}$, the analytical Jacobian is applied

$$\boldsymbol{\Delta\theta_1} = \boldsymbol{J_a}^{-1}\boldsymbol{\Delta V_1} \tag{12}$$

where

$$\boldsymbol{J_a} = \begin{bmatrix} \boldsymbol{I} & \boldsymbol{0} \\ \boldsymbol{0} & \boldsymbol{B^{-1}} \end{bmatrix} \boldsymbol{Jg} \tag{13}$$

$$\boldsymbol{B} = \begin{bmatrix} \cos(\theta_{ZR2})\sin(\theta_{YR}) & -sin(\theta_{ZR2}) & 0 \\ \sin(\theta_{ZR2})\sin(\theta_{YR})) & cos(\theta_{ZR2}) & 0 \\ \cos(\theta_{YR}) & 0 & 1 \end{bmatrix} \tag{14}$$

$\boldsymbol{J_g}$ is the geometric Jacobian of the robot. If frame $\{\boldsymbol{i}\}$ is set on joint $i+1$, $\boldsymbol{J_g}$ can be calculated as

$$\boldsymbol{Jg} = \begin{bmatrix} \boldsymbol{z_1^0} \times (\boldsymbol{o_6^0} - \boldsymbol{o_1^0}) & \boldsymbol{z_1^0} \\ \boldsymbol{z_2^0} \times (\boldsymbol{o_6^0} - \boldsymbol{o_2^0}) & \boldsymbol{z_2^0} \\ \boldsymbol{z_3^0} \times (\boldsymbol{o_6^0} - \boldsymbol{o_3^0}) & \boldsymbol{z_3^0} \\ \boldsymbol{z_4^0} \times (\boldsymbol{o_6^0} - \boldsymbol{o_4^0}) & \boldsymbol{z_4^0} \\ \boldsymbol{z_5^0} \times (\boldsymbol{o_6^0} - \boldsymbol{o_1^0}) & \boldsymbol{z_5^0} \\ \boldsymbol{z_6^0} \times (\boldsymbol{o_6^0} - \boldsymbol{o_1^0}) & \boldsymbol{z_6^0} \end{bmatrix}^T \tag{15}$$

Therefore, the target joint $\boldsymbol{\theta_{T_1}}$ value for the 2D precursor is

$$\boldsymbol{\theta_{T_1}} = \boldsymbol{\theta_R} + \boldsymbol{\Delta\theta_1} \tag{16}$$

Setting the robotic joint value as $\boldsymbol{\theta_{T_1}}$ allows the robot to bring the 2D precursor under the dispensing tip for accurate adhesive dispensing on bonding site $\boldsymbol{P_1'}$.

Fig. 7 shows the alignment processes for four bonding sites. The goal of the alignment is to use image-guided localization and positioning to overlap the 2D precursor with the four imaginary references. After two iterations, the 2D precursor and the references converges with significantly reduced errors.

This method is also used to position 2D precursors on the substrate in a desired pose for the assembly of well-aligned arrays, which is shown in Section V.

After two alignments for each bonding site, the value of $\boldsymbol{T_C^{R_i}}, i = 1, 2, 3, 4$ can be obtained. It is then applied to equation 4 to calculate the target joint values $\boldsymbol{\theta_{T_i}}, i = 1, 2, 3, 4$ for dispensing adhesive.

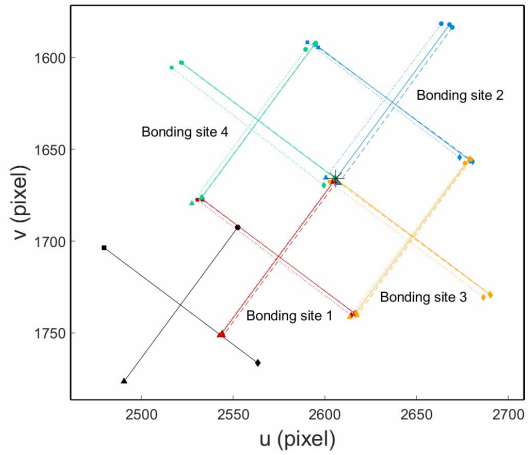

Fig. 7: Illustration of the image-guided positioning process. Star: reference; black cross: 2D precursor before alignment; colored solid cross: reference; colored dotted cross: 2D precursor after first alignment; colored dashed cross: 2D precursors after second alignment.

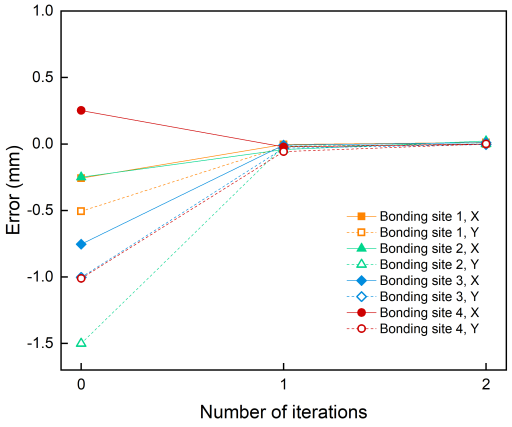

Fig. 8: Positioning errors of bonding site detection after multiple iterations.

V. Results

A. Positioning repeatability

First, the repeatability of the positioning of 2D precursors with respect to the camera is measured by driving the robot with the PDMS stamp and 2D precursors to travel between two fixed locations repeatedly. Three separate experiments are conducted and the horizontal positions of the 2D precursors measured at a target location are plotted in Fig. 9.

The repeatability of the positioning of 2D precursors with respect to the camera in our experimental setup is 0.023 mm, 0.023 mm and 0.018 mm for the 3 measurements, respectively. In addition to the repeatability of the robot (0.01 mm), vibration of the experimental setup may have also contributed to the positioning variations which could be minimized by enhancing the stability of the experimental setup.

B. Accuracy of adhesive dispensing

We perform adhesive dispensing on different 2D precursor patterns with four circular bonding sites following

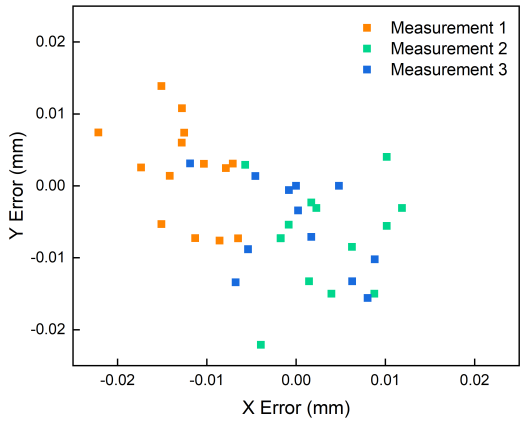

Fig. 9: Positions of the 2D precursor during positioning repeatability measurements.

the scheme described in Section IV. Fig. 10 shows optical images of representative 2D precursors after dispensing adhesive on the four bonding sites of each 2D precursor. The

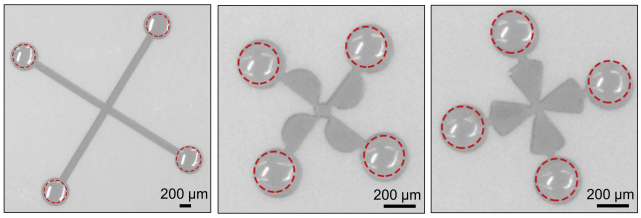

Fig. 10: Representative optical images of 2D precursors after dispensing adhesive on the bonding sites. Red circles indicate the dispensed adhesive.

dispensing error, defined as the distance between the center of the circular bonding site to the center of the dispensed adhesive, determines the effect of selected bonding between the bonding sites and the prestretched substrate. We have performed adhesive dispensing on over 70 bonding sites and the positioning errors are shown in Fig. 11. The maximum

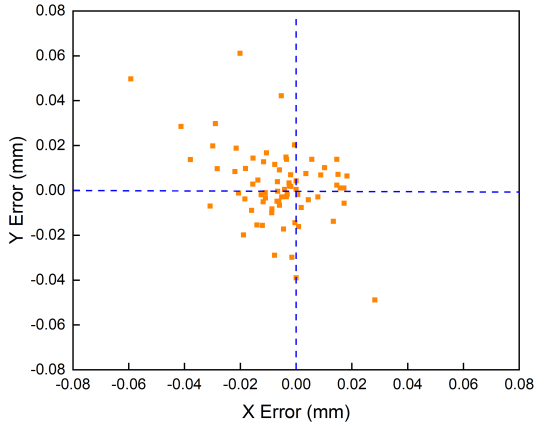

Fig. 11: Positioning accuracy measurements of adhesive dispensing on bonding sites.

error measured in the distance of the center of adhesive and the center of the bonding sites is 0.077 mm, which is sufficiently small for successful dispensing of adhesive on bonding sites that are 0.3 mm or larger in diameter. This error originates from multiple sources, including the system's repeatability (approximately 0.02 mm), the robot's positioning accuracy, errors in image detection (0.02 mm), uneven stamp surface, image-based localization and positioning, and errors associated with the contact between the dispensing tip and the 2D precursors. The dispensing error could be reduced by improving the robot's positiong accurcy, the image resolution for image-guided localization and the better control of the dispensing process.

Direction	Max (abs)/mm	Mean/mm	Std/mm
X	0.0592	-0.0064	0.0149
Y	0.0610	0.0020	0.0172
D (distance)	0.0773	0.0187	0.0146

TABLE I: Statistics of the measured dispensing errors.

C. Formation of 3D mesostructures

After dispensing the adhesive on the bonding sites, the 2D precursors are brought into contact with an elastomeric substrate which is biaxially stretched to 30% using the automatic stretcher. Such placement of 2D precursors could occur in a parallel fashion by placing multiple 2D precursors on the stamp. Bonding the 2D precursors to the substrate via adhesive curing and releasing the prestretched substrate initiate the guided mechanical buckling process. The non-bonded regions pop up to form a 3D configuration [2]. Repeating the pick-and-place operation of 2D precursors with spatial arrangements on the substrate allows for assembly of arrays of such 3D mesostructures in a single buckling step, as shown in Fig. 2. Fig. 12 presents a 3x3 array of well-aligned 3D mesostructures formed by such mechanical buckling process. The alignment of the 2D precursor array uses the alignment process shown in Fig. 7.

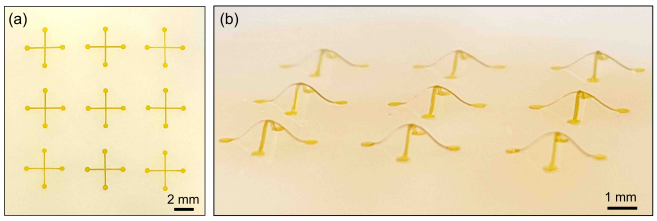

Fig. 12: Optical image of a 3x3 array of (a) 2D precursors placed on the substrate and (b) 3D mesostructures formed by automated mechanical buckling.

D. Speed of automated assembly

The operation times for selected steps of the assembly process are shown in TABLE II.

The high-speed motion of the robot allows for fast movements among different locations of the experimental setup, which significantly increases the throughput of the assembly process as compared to manual assembly. The pick and place operations can be applied to arrays of 2D precursors instead of sequential, individual operations demonstrated here. Given the one-step, parallel nature of the compressive buckling step, the entire assembly process of 3D mesostructures can operate with high throughput in an automated fashion which has the potential for mass production.

Step	Approx. operation time/s
Pickup of 2D precursor	2
Travel to camera	2
Travel to dispenser	1.5
Dispensing of adhesive (4x)	8
Travel to prestretched substrate	2
Placement of 2D precursor on substrate	1
Bonding (curing of adhesive)	60
Release of substrate	6
Return to pickup location	1.5

TABLE II: Approximate operation times for selected steps of the assembly process.

VI. Conclusions

We have demonstrated that industrial robotic manipulators can be used to automate pick and place operations needed for forming 3D mesostructures via a guided mechanical buckling process. Here is a summary of the main results presented in this paper:

- Using a 6 DOF industrial robot and a simple image-guided localizing and positioning scheme, we realized positioning accuracy of 80 μm;
- Leveraging the high repeatability of the robot, wide working space, and image-guided positioning of 6 DOF industrial robots, we demonstrated their application in automated material handling at mesoscale, specifically, in assembly of 3D mesostructures via guided mechanical buckling;
- We realized fully automated, fast assembly of 3D mesostructures via guided mechanical buckling without manual intervention.

The approach presented in this study provides a means of achieving hybrid micro-scale devices of high complexity while maintaining high yield and low cost, which may find applications in small-scale manufacturing include micromachining, assembly of microelectronics, additive manufacturing, robotic surgery, and many others [9], [13], [23], [24]. We plan to further improve the system's positioning accuracy by enhancing the robot's positioning accuracy, optimizing the image resolution and experimental setup, as well as incorporating multi-level perception for robotic manipulation at smaller length scales.

Acknowledgements: We acknowledge the support from Yaskawa America, Inc. Hangbo Zhao acknowledges the startup support from the Viterbi School of Engineering at University of Southern California.

References

[1] Y. Zhang, F. Zhang, Z. Yan, Q. Ma, X. Li, Y. Huang, and J. A. Rogers, "Printing, folding and assembly methods for forming 3d mesostructures in advanced materials," *Nature Reviews Materials*, vol. 2, no. 4, p. 17019, 2017.

[2] S. Xu, Z. Yan, K.-I. Jang, W. Huang, H. Fu, J. Kim, Z. Wei, M. Flavin, J. McCracken, R. Wang, A. Badea, Y. Liu, D. Xiao, G. Zhou, J. Lee, H. U. Chung, H. Cheng, W. Ren, A. Banks, X. Li, U. Paik, R. G. Nuzzo, Y. Huang, Y. Zhang, and J. A. Rogers, "Assembly of micro/nanomaterials into complex, three-dimensional architectures

by compressive buckling," *Science*, vol. 347, no. 6218, pp. 154–159, 2015.

[3] Z. Yan, M. Han, Y. Yang, K. Nan, H. Luan, Y. Luo, Y. Zhang, Y. Huang, and J. A. Rogers, "Deterministic assembly of 3d mesostructures in advanced materials via compressive buckling: A short review of recent progress," *Extreme Mechanics Letters*, vol. 11, pp. 96 – 104, 2017. [Online]. Available: http://www.sciencedirect.com/science/article/pii/S2352431616302218

[4] M. Han, H. Wang, Y. Yang, C. Liang, W. Bai, Z. Yan, H. Li, Y. Xue, X. Wang, B. Akar, H. Zhao, H. Luan, J. Lim, I. Kandela, G. A. Ameer, Y. Zhang, Y. Huang, Y. Zhang, and J. A. Rogers, "Three-dimensional piezoelectric polymer microsystems for vibrational energy harvesting, robotic interfaces and biomedical implants," *Nature Electronics*, vol. 2, pp. 26–35, 2018.

[5] H. Zhao, K. Li, M. Han, F. Zhu, A. Vázquez-Guardado, P. Guo, Z. Xie, Y. Park, L. Chen, X. Wang, H. Luan, Y. Yang, H. Wang, C. Liang, Y. Xue, R. D. Schaller, D. Chanda, Y. Huang, Y. Zhang, and J. A. Rogers, "Buckling and twisting of advanced materials into morphable 3d mesostructures," *Proceedings of the National Academy of Sciences*, vol. 116, no. 27, pp. 13 239–13 248, 2019.

[6] Z. Yan, M. Han, Y. Shi, A. Badea, Y. Yang, A. Kulkarni, E. Hanson, M. E. Kandel, X. Wen, F. Zhang, Y. Luo, Q. Lin, H. Zhang, X. Guo, Y. Huang, K. Nan, S. Jia, A. W. Oraham, M. B. Mevis, J. Lim, X. Guo, M. Gao, W. Ryu, K. J. Yu, B. G. Nicolau, A. Petronico, S. S. Rubakhin, J. Lou, P. M. Ajayan, K. Thornton, G. Popescu, D. Fang, J. V. Sweedler, P. V. Braun, H. Zhang, R. G. Nuzzo, Y. Huang, Y. Zhang, and J. A. Rogers, "Three-dimensional mesostructures as high-temperature growth templates, electronic cellular scaffolds, and self-propelled microrobots," *Proceedings of the National Academy of Sciences*, vol. 114, no. 45, pp. E9455–E9464, 2017. [Online]. Available: https://www.pnas.org/content/114/45/E9455

[7] X. Wang, R. Feiner, H. Luan, Q. Zhang, S. Zhao, Y. Zhang, M. Han, Y. Li, R. Sun, H. Wang, T.-L. Liu, X. Guo, H. Oved, N. Noor, A. Shapira, Y. Zhang, Y. Huang, T. Dvir, and J. A. Rogers, "Three-dimensional electronic scaffolds for monitoring and regulation of multifunctional hybrid tissues," *Extreme Mechanics Letters*, vol. 35, p. 100634, 2020. [Online]. Available: http://www.sciencedirect.com/science/article/pii/S2352431620300092

[8] H. Zhao, Y. Kim, H. Wang, X. Ning, C. Xu, J. Suh, M. Han, G. J. Pagan-Diaz, W. Lu, H. Li, W. Bai, O. Aydin, Y. Park, J. Wang, Y. Yao, Y. He, M. T. A. Saif, Y. Huang, R. Bashir, and J. A. Rogers, "Compliant 3d frameworks instrumented with strain sensors for characterization of millimeter-scale engineered muscle tissues," *Proceedings of the National Academy of Sciences*, vol. 118, no. 19, 2021. [Online]. Available: https://www.pnas.org/content/118/19/e2100077118

[9] P. M. Bhatt, R. K. Malhan, A. V. Shembekar, Y. J. Yoon, and S. K. Gupta, "Expanding capabilities of additive manufacturing through use of robotics technologies: A survey," *Additive Manufacturing*, vol. 31, p. 100933, 2020. [Online]. Available: https://www.sciencedirect.com/science/article/pii/S2214860419312266

[10] B. Tamadazte, N. L. Piat, and S. Dembélé, "Robotic micromanipulation and microassembly using monoview and multiscale visual servoing," *IEEE/ASME Transactions on Mechatronics*, vol. 16, no. 2, pp. 277–287, 2011.

[11] Y. Zhang, "Vision servo of industrial robot: A review," *AIP Conference Proceedings*, vol. 1955, no. 1, p. 040125, 2018. [Online]. Available: https://aip.scitation.org/doi/abs/10.1063/1.5033789

[12] I. Fassi and D. Shipley, "Micro-manufacturing technologies and their applications," *Springer Tracts in Mechanical Engineering*, vol. 10, pp. 978–3, 2017.

[13] Z. Zhang, X. Wang, J. Liu, C. Dai, and Y. Sun, "Robotic micromanipulation: Fundamentals and applications," *Annual Review of Control, Robotics, and Autonomous Systems*, vol. 2, pp. 181–203, 2019.

[14] N. Ahmed, A. Carlson, J. A. Rogers, and P. M. Ferreira, "Automated micro-transfer printing with cantilevered stamps," *Journal of Manufacturing Processes*, vol. 14, no. 2, pp. 90–97, 2012, micro and Nano Manufacturing. [Online]. Available: https://www.sciencedirect.com/science/article/pii/S1526612511000363

[15] D. J. Cappelleri, M. Fatovic, and U. Shah, "Caging micromanipulation for automated microassembly," in *2011 IEEE International Conference on Robotics and Automation*, 2011, pp. 3145–3150.

[16] J. D. Wason, J. T. Wen, J. J. Gorman, and N. G. Dagalakis, "Automated multiprobe microassembly using vision feedback," *IEEE Transactions on Robotics*, vol. 28, no. 5, pp. 1090–1103, 2012.

[17] B. Komati, A. Kudryavtsev, C. Clévy, G. Laurent, B. Tamadazte, J. Agnus, and P. Lutz, "Automated robotic microassembly of flexible optical components," in *2016 IEEE International Symposium on Assembly and Manufacturing (ISAM)*. IEEE, 2016, pp. 93–98.

[18] V. Venkatesan and D. J. Cappelleri, "Development of an automated flexible micro-soldering station," in *International Design Engineering Technical Conferences and Computers and Information in Engineering Conference*, vol. 58165. American Society of Mechanical Engineers, 2017, p. V004T09A023.

[19] S. Ruggeri, G. Fontana, V. Basile, M. Valori, and I. Fassi, "Micro-robotic handling solutions for pcb (re-)manufacturing," *Procedia Manufacturing*, vol. 11, pp. 441–448, 2017, 27th International Conference on Flexible Automation and Intelligent Manufacturing, FAIM2017, 27-30 June 2017, Modena, Italy. [Online]. Available: https://www.sciencedirect.com/science/article/pii/S2351978917303360

[20] L. Niu, M. Saarinen, R. Tuokko, and J. Mattila, "Integration of multi-camera vision system for automatic robotic assembly," *Procedia Manufacturing*, vol. 37, pp. 380–384, 2019, physical and Numerical Simulation of Materials Processing IX. [Online]. Available: https://www.sciencedirect.com/science/article/pii/S2351978919312697

[21] Y. Ma, K. Du, D. Zhou, J. Zhang, X. Liu, and D. Xu, "Automatic precision robot assembly system with microscopic vision and force sensor," *International Journal of Advanced Robotic Systems*, vol. 16, no. 3, p. 1729881419851619, 2019. [Online]. Available: https://doi.org/10.1177/1729881419851619

[22] Y. Cai, Z. Han, T. Cranney, H. Zhao, and S. K. Gupta. (2021) Automated robotic assembly of 3d mesostructure via guided mechanical buckling. [Online]. Available: https://youtu.be/0I3MJpjec_M

[23] I. Fassi and D. Shipley, "Micro-manufacturing technologies and their applications," *Springer Tracts in Mechanical Engineering*, vol. 10, pp. 978–3, 2017.

[24] Y. Tian, M. Draelos, G. Tang, R. Qian, A. Kuo, J. Izatt, and K. Hauser, "Toward autonomous robotic micro-suturing using optical coherence tomography calibration and path planning," in *2020 IEEE International Conference on Robotics and Automation (ICRA)*, 2020, pp. 5516–5522.